

Giant Anisotropy of Gilbert Damping in Epitaxial CoFe Films

Yi Li,^{1,2} Fanlong Zeng,³ Steven S.-L. Zhang,² Hyeondeok Shin,⁴ Hilal Saglam,^{2,5} Vedat Karakas,^{2,6} Ozhan Ozatay,^{2,6} John E. Pearson,² Olle G. Heinonen,² Yizheng Wu,^{3,7,*} Axel Hoffmann,^{2,†} and Wei Zhang^{1,2,‡}

¹*Department of Physics, Oakland University, Rochester, Michigan 48309, USA*

²*Materials Science Division, Argonne National Laboratory, Argonne, Illinois 60439, USA*

³*State Key Laboratory of Surface Physics, Department of Physics, Fudan University, Shanghai 200433, China*

⁴*Computational Sciences Division, Argonne National Laboratory, Argonne, Illinois 60439, USA*

⁵*Department of Physics, Illinois Institute of Technology, Chicago Illinois 60616, USA*

⁶*Department of Physics, Bogazici University, Bebek 34342, Istanbul, Turkey*

⁷*Collaborative Innovation Center of Advanced Microstructures, Nanjing 210093, China*

 (Received 13 July 2018; revised manuscript received 30 November 2018; published 21 March 2019)

Tailoring Gilbert damping of metallic ferromagnetic thin films is one of the central interests in spintronics applications. Here we report a giant Gilbert damping anisotropy in epitaxial $\text{Co}_{50}\text{Fe}_{50}$ thin films with a maximum-minimum damping ratio of 400%, determined by broadband spin-torque ferromagnetic resonance as well as inductive ferromagnetic resonance. We conclude that the origin of this damping anisotropy is the variation of the spin orbit coupling for different magnetization orientations in the cubic lattice, which is further corroborated from the magnitude of the anisotropic magnetoresistance in $\text{Co}_{50}\text{Fe}_{50}$.

DOI: [10.1103/PhysRevLett.122.117203](https://doi.org/10.1103/PhysRevLett.122.117203)

In magnetization dynamics the energy relaxation rate is quantified by the phenomenological Gilbert damping in the Landau-Lifshits-Gilbert equation [1], which is a key parameter for emerging spintronics applications [2–6]. Being able to design and control the Gilbert damping on demand is crucial for versatile spintronic device engineering and optimization. For example, lower damping enables more energy-efficient excitations, while larger damping allows faster relaxation to equilibrium and more favorable latency. Nevertheless, despite abundant approaches including interfacial damping enhancement [7–9], size effect [10,11], and materials engineering [12–14], there has not been much progress on how to manipulate damping within the same magnetic device. The only well-studied damping manipulation is by spin torque [15–18], which can even fully compensate the intrinsic damping [19,20]. However the requirement of large current density narrows its applied potential.

An alternative approach is to explore the intrinsic Gilbert damping anisotropy associated with the crystalline symmetry, where the damping can be continuously tuned via rotating the magnetization orientation. Although there are many theoretical predictions [21–25], most early studies of damping anisotropy are disguised by two-magnon scattering and linewidth broadening due to field-magnetization misalignment [26–29]. In addition, those reported effects are usually too weak to be considered in practical applications [30,31].

In this work, we show that a metallic ferromagnet can exhibit a giant Gilbert damping variation by a factor of 4 along with low minimum damping. We investigated

epitaxial cobalt-iron alloys, which have demonstrated new potentials in spintronics due to their ultralow dampings [32,33]. Using spin-torque-driven and inductive ferromagnetic resonance (FMR), we obtain a fourfold (cubic) damping anisotropy of 400% in $\text{Co}_{50}\text{Fe}_{50}$ thin films between their easy and hard axes. For each angle, the full-range frequency dependence of FMR linewidths can be well reproduced by a single damping parameter α . Furthermore, from first-principles calculations and temperature-dependent measurements, we argue that this giant damping anisotropy in $\text{Co}_{50}\text{Fe}_{50}$ is due to the variation of the spin-orbit coupling (SOC) in the cubic lattice, which differs from the anisotropic density of state found in ultrathin Fe film [30]. We support our conclusion by comparing the Gilbert damping with the anisotropic magnetoresistance (AMR) signals. Our results reveal the key mechanism to engineer the Gilbert damping and may open a new pathway to develop novel functionality in spintronic devices.

$\text{Co}_{50}\text{Fe}_{50}$ (CoFe) films were deposited on MgO(100) substrates by molecular beam epitaxy at room temperature, under a base pressure of 2×10^{-10} Torr [34]. For spin-torque FMR measurements, (i) $\text{CoFe}(10 \text{ nm})|\text{Pt}(6 \text{ nm})$ and (ii) $\text{CoFe}(10 \text{ nm})$ samples were prepared. They were fabricated into $10 \mu\text{m} \times 40 \mu\text{m}$ bars by photolithography and ion milling. Coplanar waveguides with 100-nm thick Au were subsequently fabricated [18,35]. For each layer structure, 14 devices with different orientations were fabricated, as shown in Fig. 1(a). The geometry defines the orientation of the microwave current θ_I and the orientation of the biasing field θ_H with respect to the MgO [100] axis (CoFe [1 $\bar{1}$ 0]). θ_I

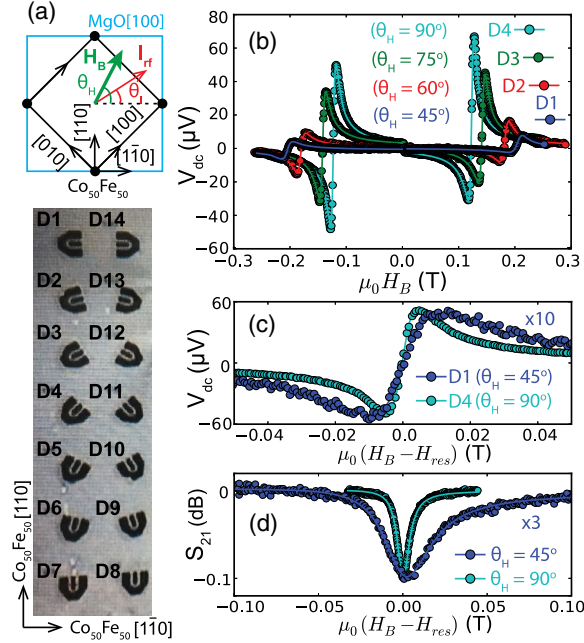


FIG. 1. (a) Upper: crystalline structure, axes of bcc $\text{Co}_{50}\text{Fe}_{50}$ film on $\text{MgO}(100)$ substrate, and definition of θ_H and θ_I . Lower: device orientation with respect to the CoFe crystal axis. (b) Spin-torque FMR line shapes of (i) $\text{CoFe}(10\text{ nm})|\text{Pt}$ devices D1 to D4 measured. (c) Resonances of D1 and D4 from (b) for $\mu_0 H_{\text{res}} < 0$. (d) Resonances of (iii) $\text{CoFe}(20\text{ nm})$ for $\theta_H = 45^\circ$ and 90° measured by VNA FMR. In (b)–(d) $\omega/2\pi = 20\text{ GHz}$ and offset applies.

ranges from 0° to 180° with a step of 15° (D1 to D14, with D7 and D8 pointing to the same direction). For each device we fix $\theta_H = \theta_I + 45^\circ$ for maximal rectification signals. In addition, we also prepared (iii) $\text{CoFe}(20\text{ nm})$ $40\ \mu\text{m} \times 200\ \mu\text{m}$ bars along different orientations with transmission coplanar waveguides fabricated on top for vector network analyzer (VNA) measurements. See the Supplemental Material for details [36].

Figure 1(b) shows the angular-dependent spin-torque FMR line shapes of $\text{CoFe}(10\text{ nm})|\text{Pt}$ devices from different samples (D1 to D4, hard axis to easy axis) at $\omega/2\pi = 20\text{ GHz}$. A strong magnetocrystalline anisotropy as well as a variation of resonance signals are observed. Moreover, the linewidth increases significantly from easy axis to hard axis, which is shown in Fig. 1(c). We have also conducted rotating-field measurements on a second $\text{CoFe}(10\text{ nm})|\text{Pt}$ device from a different deposition and the observations can be reproduced. This linewidth anisotropy is even more pronounced for the $\text{CoFe}(20\text{ nm})$ devices without Pt, measured by VNA FMR [Fig. 1(d)]. For the $\text{CoFe}(10\text{ nm})$ devices, due to the absence of the Pt spin injector the spin-torque FMR signals are much weaker than $\text{CoFe}|\text{Pt}$ and completely vanish when the microwave current is along the easy axes.

Figures 2(a)–2(b) show the angular and frequency dependence of the resonance field H_{res} . In Fig. 2(a), the

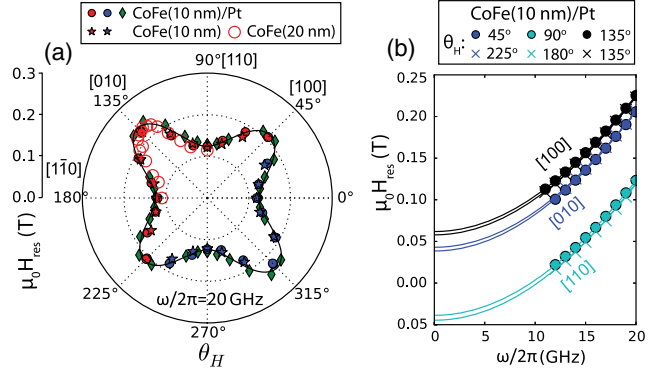


FIG. 2. (a) Resonance field $\mu_0 H_{\text{res}}$ as a function of θ_H at $\omega/2\pi = 20\text{ GHz}$ for different samples. Diamonds denote the rotating-field measurement from the second $\text{CoFe}(10\text{ nm})|\text{Pt}$ device. The black curve denotes the theoretical prediction. (b) $\mu_0 H_{\text{res}}$ as a function of frequency for the $\text{CoFe}(10\text{ nm})|\text{Pt}$ devices. Solid curves denote the fits to the Kittel equation.

H_{res} for all four sample series match with each other, which demonstrates that the magnetocrystalline properties of $\text{CoFe}(10\text{ nm})$ samples are reproducible. A slightly smaller H_{res} for $\text{CoFe}(20\text{ nm})$ is caused by a greater effective magnetization when the thickness increases. A clear four-fold symmetry is observed, which is indicative of the cubic lattice due to the body-center-cubic (bcc) texture of $\text{Co}_{50}\text{Fe}_{50}$ on MgO . We note that the directions of the hard axes switched from $[100]$ and $[010]$ in iron-rich alloys [33] to $[110]$ and $[1\bar{1}0]$ in $\text{Co}_{50}\text{Fe}_{50}$, which is consistent with previous reports [39,40].

The magnetocrystalline anisotropy can be quantified from the frequency dependence of $\mu_0 H_{\text{res}}$. Figure 2(b) shows the results of $\text{CoFe}(10\text{ nm})|\text{Pt}$ when H_B is aligned to the easy and hard axes. A small uniaxial anisotropy is found between $[1\bar{1}0]$ (0° and 180°) and $[110]$ (90°) axes. By fitting the data to the Kittel equation $\omega^2/\gamma^2 = \mu_0^2(H_{\text{res}} - H_k) \times (H_{\text{res}} - H_k + M_s)$, where $\gamma = 2\pi(g_{\text{eff}}/2) \times 28\text{ GHz/T}$, we obtain $g_{\text{eff}} = 2.16$, $\mu_0 M_s = 2.47\text{ T}$, $\mu_0 H_k^{[100]} = 40\text{ mT}$, $\mu_0 H_k^{[010]} = 65\text{ mT}$, and $\mu_0 H_k^{[110]} = \mu_0 H_k^{[1\bar{1}0]} = -43\text{ mT}$. Taking the dispersion functions from cubic magnetocrystalline anisotropy [41,42], we obtain an in-plane cubic anisotropy field $\mu_0 H_{4||} = 48\text{ mT}$ and a uniaxial anisotropy field $\mu_0 H_{2||} = 12\text{ mT}$. Figure 2(a) shows the theoretical predictions from $H_{4||}$ and $H_{2||}$ in black curve, which aligns well with all 10-nm CoFe samples.

With good magnetocrystalline properties, we now turn to the energy relaxation rate. Figure 3(a) shows the full-width-half-maximum linewidths $\mu_0 \Delta H_{1/2}$ of the spin-torque FMR signals at $\omega/2\pi = 20\text{ GHz}$. Again, a fourfold symmetry is observed for $\text{CoFe}(10\text{ nm})|\text{Pt}$ and $\text{CoFe}(10\text{ nm})$, with the minimal (maximal) linewidth measured when the field lies along the easy (hard) axes. For $\text{CoFe}(10\text{ nm})$ devices, we did not measure any spin-torque FMR signal for H_B along the hard axes ($\theta_H = 45^\circ, 135^\circ$ and 225°). This is due to the

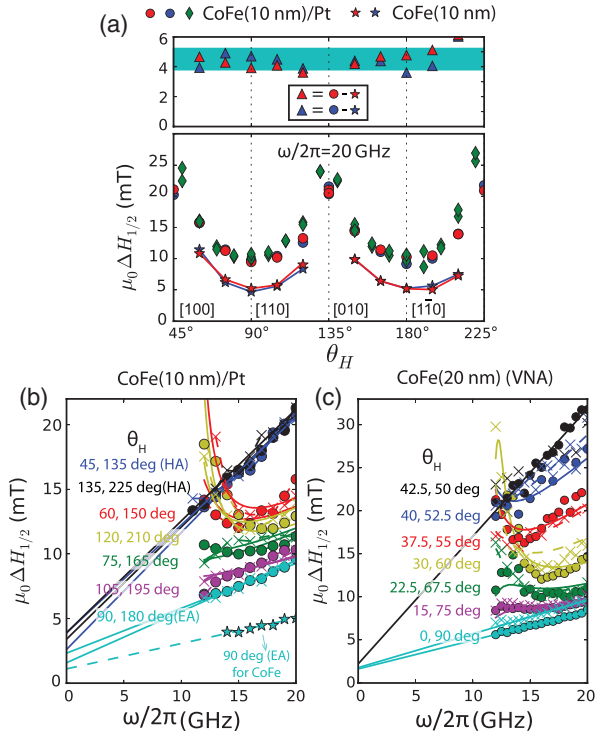


FIG. 3. (a) $\mu_0\Delta H_{1/2}$ as a function of θ_H at $\omega/2\pi = 20$ GHz for the CoFe(10 nm) series in Fig. 2(a). Top: Additional linewidth due to spin pumping of Pt. The green region denotes the additional linewidth as 4.5 ± 0.7 mT. (b)–(c) $\mu_0\Delta H_{1/2}$ as a function of frequency for (b) CoFe(10 nm)|Pt and (c) CoFe(20 nm) samples. Solid lines and curves are the fits to the data.

absence of the Pt spin injector as well as the near-zero AMR ratio when the rf current flows along the easy axes, which will be discussed later. For all other measurements, the linewidths of CoFe devices are smaller than for CoFe|Pt by the same constant, independent of orientation [upper diagram of Fig. 3(a)]. This constant linewidth difference is due to the spin pumping contribution to damping from the additional Pt layer [43,44]. Thus we can deduce the intrinsic damping anisotropy from CoFe(10 nm)|Pt devices, with the damping shifted from CoFe(10 nm) devices by a constant and with much easier measurements.

In Fig. 3(b)–3(c) we show the frequency dependence of $\mu_0\Delta H_{1/2}$ of CoFe(10 nm)|Pt devices from spin-torque FMR and CoFe(20 nm) devices from VNA FMR. For both the easy and hard axes, linear relations are obtained, and the Gilbert damping α can be extracted from $\mu_0\Delta H_{1/2} = \mu_0\Delta H_0 + 2\alpha\omega/\gamma$ with the fits shown as solid lines. Here $\mu_0\Delta H_0$ is the inhomogeneous broadening due to the disorders in lattice structures. In Fig. 3(b) we also show the linewidths of the CoFe(10 nm) device along the easy axis ($\theta_H = 90^\circ$), which has a significant lower linewidth slope than the easy axis of CoFe(10 nm)|Pt. Their differences yield a spin pumping damping contribution of $\Delta\alpha_{sp} = 0.0024$. By using $\Delta\alpha_{sp} = \gamma\hbar g^{\uparrow\downarrow}/(4\pi M_s t_M)$,

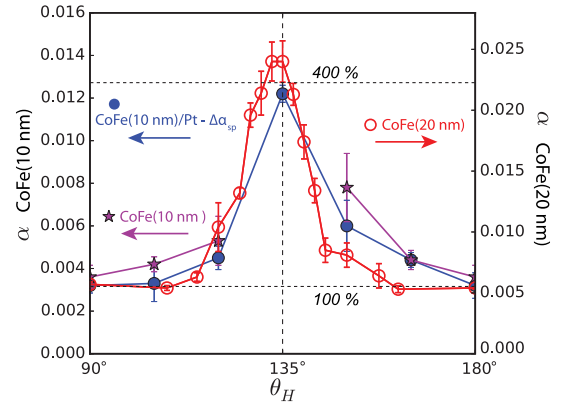


FIG. 4. Renormalized damping and its anisotropy for CoFe(10 nm) and CoFe(20 nm), measured from spin-torque FMR and VNA FMR, respectively. For CoFe(20 nm)|Pt samples, $\Delta\alpha_{sp}$ has been subtracted from the measured damping.

obtain a spin mixing conductance of $g^{\uparrow\downarrow}(\text{CoFe|Pt}) = 25 \text{ nm}^{-2}$, which is comparable to similar interfaces such as NiFe|Pt [45,46]. For θ_H between the easy and hard axes, the low-frequency linewidth broadenings are caused by the deviation of magnetization from the biasing field direction, whereas at high frequencies the field is sufficient to saturate the magnetization. In order to find the damping anisotropy, we fit the linewidths to the angular model developed by Suhl [47,48], using a single fit parameter of α and the extracted $H_{2||}$ and $H_{4||}$ from Fig. 2. The solid fitting curves in Fig. 3(b) nicely reproduce the experimental points.

The obtained damping anisotropy for all the samples are summarized in Fig. 4, which is the main result of the Letter. For CoFe(10 nm)|Pt samples, α varies from 0.0056 along the easy axis to 0.0146 along the hard axis. By subtracting the spin pumping $\Delta\alpha_{sp}$ from both values, we derive a damping anisotropy of 380%. For CoFe(20 nm) samples measured by VNA FMR, α varies from 0.0054 to 0.0240, which yields an anisotropy of 440% and reproduces the large anisotropy from spin-torque FMR. This giant damping anisotropy implies, technologically, nearly 4 times smaller critical current to switch the magnetization in a spin-torque magnetic random access memory, or to excite auto-oscillation in a spin-torque oscillator, by simply changing the magnetization orientation from the hard axis to the easy axis within the same device. In addition, we emphasize that our reported damping anisotropy is not subject to a dominant two-magnon scattering contribution, which would be manifested as a nonlinear linewidth softening at high frequencies [28,31]. For this purpose we have extended the frequency of spin-torque FMR on CoFe(10 nm)|Pt up to 39 GHz; see the Supplemental Material for details [36]. We choose CoFe(10 nm)|Pt samples because they provide the best signals at high frequencies and the additional Pt layer significantly helps to excite the dynamics. Linear frequency dependence of linewidth persists throughout the frequency range and ΔH_0

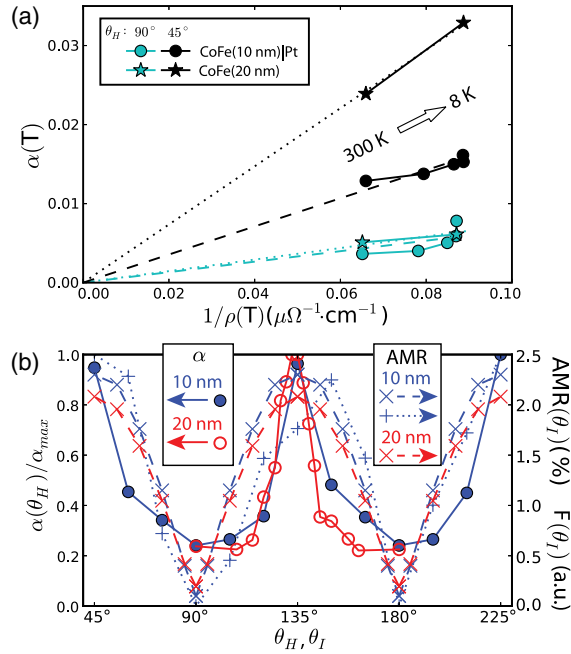


FIG. 5. (a) $\alpha(T)$ as a function of $1/\rho(T)$. $T = 8, 30, 70, 150,$ and 300 K for CoFe(10 nm)|Pt and $T = 8$ and 300 K for CoFe(20 nm). Dashed and dotted lines are guides to eyes. (b) Renormalized $\alpha(\theta_H)$, AMR(θ_I), and $F(\theta_I)$ for CoFe(10 nm)|Pt and CoFe(20 nm). Circles denote α ; crosses and pluses denote AMR and F , respectively.

is unchanged for the two axes, with which we can exclude extrinsic effects to the linewidths. We also note that our result is substantially different from the recent report on damping anisotropy in Fe|GaAs [30], which is due to the interfacial SOC and disappears quickly as Fe becomes thicker. In comparison, the Gilbert damping anisotropy in $\text{Co}_{50}\text{Fe}_{50}$ is the intrinsic property of the material, is bonded to its bulk crystalline structure, and thus holds for different thicknesses in our experiments.

In order to investigate the dominant mechanism for such a large Gilbert damping anisotropy, we perform temperature-dependent measurements of α and the resistivity ρ . Figure 5(a) plots α as a function of $1/\rho$ for the CoFe(10 nm)|Pt and CoFe(20 nm) samples and for H_B along the easy and hard axes. The dominant linear dependence reveals a major role of conductivitylike damping behavior. This is described by the breathing Fermi surface model for transition-metal ferromagnets, in which α can be expressed as [23,24,49–51]

$$\alpha \sim N(E_F)|\Gamma^-|^2\tau, \quad (1)$$

where $N(E_F)$ is the density of state at the Fermi level, τ is the electron relaxation time, and $\Gamma^- = \langle[\sigma^-, H_{so}]\rangle_{E=E_F}$ is the matrix for spin-flip scatterings induced by the SOC Hamiltonian H_{so} near the Fermi surface [50,51]. Here τ is proportional to the conductivity ($1/\rho$) from the Drude

model, with which Eq. (1) gives rise to the behaviors shown in Fig. 5(a).

For the origin of damping anisotropy, we first check the role of $N(E_F)$ by *ab initio* calculations for different ordered cubic supercells, which is shown in the Supplemental Material [36]. However, a negligible anisotropy in $N(E_F)$ is found for different magnetization orientations. This is consistent with the calculated anisotropy in Ref. [30], where less than 0.4% change of $N(E_F)$ was obtained in ultrathin Fe films. The role of τ can also be excluded from the fact that the resistivity difference between the easy and hard axes is less than 2% [36]. Thus we deduce that the giant damping anisotropy of 400% is due to the change of $|\Gamma^-|^2$, or the SOC, at different crystalline directions. In particular, unlike the single element Fe, disordered bcc Fe-Co alloy can possess atomic short-range order, which gives rise to local tetragonal crystal distortions due to the different lattice constants of Fe and Co [52–54]. Such local tetragonal distortions will preserve global cubic symmetry but can have large effects on the SOC. We emphasize that our CoFe samples, which did not experience annealing, preserve the random disorder. Our first-principles calculations also confirm the role of local tetragonal distortions and its enhancement on SOC; see the Supplemental Material for details [36].

The anisotropy of the SOC in $\text{Co}_{50}\text{Fe}_{50}$ can be reflected by its AMR variation along different crystalline orientations. The AMR ratio can be defined as

$$AMR(\theta_I) = \frac{\rho_{\parallel}(\theta_I)}{\rho_{\perp}(\theta_I)} - 1, \quad (2)$$

where $\rho_{\parallel}(\theta_I)$ and $\rho_{\perp}(\theta_I)$ are measured for the biasing field parallel and perpendicular to the current direction, respectively. The main contribution of AMR is the asymmetric *s-d* electron scatterings where the *s* orbitals are mixed with magnetization-containing *d* orbitals due to SOC [55,56]. Since both the damping and AMR originate from SOC and, more precisely, are proportional to the second order of SOC, a large damping anisotropy is expected to be accompanied by a large AMR anisotropy and vice versa. Furthermore, due to the fourfold symmetry, the AMR should be invariant when the current direction is rotated by 90° degrees, as the AMR is a function of θ_I as defined in Eq. (1). Thus the damping and AMR should exhibit similar angular dependence on θ_H and θ_I , respectively.

In Fig. 5(b) we compare renormalized $\alpha(\theta_H)$ with AMR(θ_I) for 10 and 20 nm CoFe samples, where the AMR values are measured from Hall bars with different θ_I . The AMR ratio is maximized along $\langle 100 \rangle$ axes and minimized along $\langle 110 \rangle$ axes, with a large anisotropy by a factor of 10. This anisotropy is also shown by the integrated spin-torque FMR intensity for CoFe(10 nm)|Pt, defined as $F(\theta_I) = \Delta H_{1/2} V_{dc}^{\max}$ [17,18] and plotted in Fig. 5(b). The large AMR anisotropy and its symmetry clearly coincide

with the damping anisotropy measured in the same samples, which confirms our hypothesis of strong SOC anisotropy in CoFe. Thus we conclude that the damping anisotropy is dominated by the variation of SOC term in Eq. (1). This effect should be much weaker for single-element epitaxial Fe, which is known to exhibit only weak damping anisotropy [30]. Experimentally we have also measured the damping and AMR anisotropies of epitaxial Fe(10 nm) films grown on GaAs substrates and we find both anisotropies less than 30% [36], which is in agreement with the damping anisotropy mechanism.

We compare our results with prior theoretical works on damping anisotropy [23,24]. First, despite their proportional relationship in Fig. 5(a), the giant anisotropy in α is not reflected in $1/\rho$. This is because the s - d scattering, which dominates in the anisotropic AMR, only contributes a small portion to the total resistivity. Second, neither the anisotropy of damping nor AMR are sensitive to temperature. This is likely because the thermal excitations at room temperature (~ 0.025 eV) are much smaller than the spin-orbit coupling (~ 0.1 eV [49]). Third, the damping tensor has been expressed as a function of \mathbf{M} and $d\mathbf{M}/dt$ [24]. However, in a fourfold-symmetry lattice and considering the large precession ellipticity, these two vectors are mostly perpendicular to each other, point towards equivalent crystalline directions, and contribute equivalently to the symmetry of damping anisotropy.

In summary, we have experimentally demonstrated very large Gilbert damping anisotropy up to 400% in epitaxial $\text{Co}_{50}\text{Fe}_{50}$ thin-film devices which follows their bulk, cubic crystalline anisotropy. We show that the damping anisotropy can be explained by the change of spin-orbit coupling within the breathing Fermi surface model, which can be probed by the corresponding AMR change. Our results provide new insights to the damping mechanism in metallic ferromagnets, which are important for optimizing dynamic properties of future magnetic devices.

We are grateful for fruitful discussions with Bret Heinrich. W. Z. acknowledges support from the U.S. National Science Foundation under Grant No. DMR-1808892, Michigan Space Grant Consortium, and DOE Visiting Faculty Program. Work at Argonne, including transport measurements and theoretical modeling, was supported by the U.S. Department of Energy, Office of Science, Materials Science and Engineering Division, and H. S. (first-principles calculations) acknowledges its Computational Materials Sciences Program's Center for Predictive Simulation of Functional Materials, the Innovative and Novel Computational Impact on Theory and Experiment (INCITE) Program, and the Argonne Leadership Computing Facility, a U.S. DOE facility under Contract No. DE-AC02-06CH11357. Work at Fudan, including thin film growth and fabrication, was supported by the National Key Basic Research Program (2015CB921401), National Key Research and Development Program (2016YFA0300703), NSFC

(11734006,11474066,11434003), and the Program of Shanghai Academic Research Leader (17XD1400400) of China. O. O. and V. K. acknowledge support from Bogazici University Research Fund (17B03D3), TUBITAK 2214/A, and the U.S. Department of State Fulbright Visiting Scholar Program.

*wuyizheng@fudan.edu.cn

†hoffmann@anl.gov

‡weizhang@oakland.edu

- [1] T. L. Gilbert, *IEEE Trans. Magn.* **40**, 3443 (2004).
- [2] S. Mangin, D. Ravelosona, J. A. Katine, M. J. Carey, B. D. Terris, and E. E. Fullerton, *Nat. Mater.* **5**, 210 (2006).
- [3] S. I. Kiselev, J. C. Sankey, I. N. Krivorotov, N. C. Emley, R. J. Schoelkopf, R. A. Buhrman, and D. C. Ralph, *Nature (London)* **425**, 380 (2003).
- [4] A. Dussaux, B. Georges, J. Grollier, V. Cros, A. V. Khvalkovskiy, A. Fukushima, M. Konoto, H. Kubota, K. Yakushiji, S. Yuasa, K. A. Zvezdin, K. Ando, and A. Fert, *Nat. Commun.* **1**, 8 (2010).
- [5] A. V. Chumak, V. I. Vasyuchka, A. A. Serga, and B. Hillebrands, *Nat. Phys.* **11**, 453 (2015).
- [6] I. M. Miron, T. Moore, H. Szabolcs, L. D. Buda-Prejbeanu, S. Auffret, B. Rodmacq, S. Pizzini, J. Vogel, M. Bonfim, A. Schuhl, and G. Gaudin, *Nat. Mater.* **10**, 419 (2011).
- [7] R. Urban, G. Woltersdorf, and B. Heinrich, *Phys. Rev. Lett.* **87**, 217204 (2001).
- [8] S. Mizukami, Y. Ando, and T. Miyazaki, *Phys. Rev. B* **66**, 104413 (2002).
- [9] Y. Tserkovnyak, A. Brataas, G. E. W. Bauer, and B. I. Halperin, *Rev. Mod. Phys.* **77**, 1375 (2005).
- [10] H. T. Nembach, J. M. Shaw, C. T. Boone, and T. J. Silva, *Phys. Rev. Lett.* **110**, 117201 (2013).
- [11] Y. Li and W. E. Bailey, *Phys. Rev. Lett.* **116**, 117602 (2016).
- [12] F. Schreiber, J. Pflaum, Z. Frait, T. Mühge, and J. Pelzl, *Solid State Commun.* **93**, 965 (1995).
- [13] M. Oogane, T. Wakitani, S. Yakata, R. Yilgin, Y. Ando, A. Sakuma, and T. Miyazaki, *Jpn. J. Appl. Phys.* **45**, 3889 (2006).
- [14] C. Shecke, L. Cheng, I. Barsukov, Z. Frait, and W. E. Bailey, *Phys. Rev. Lett.* **98**, 117601 (2007).
- [15] K. Ando, S. Takahashi, K. Harii, K. Sasage, J. Ieda, S. Maekawa, and E. Saitoh, *Phys. Rev. Lett.* **101**, 036601 (2008).
- [16] Z. Wang, Y. Sun, Y.-Y. Song, M. Wu, H. Schultheiß, J. E. Pearson, and A. Hoffmann, *Appl. Phys. Lett.* **99**, 162511 (2011).
- [17] L. Liu, T. Moriyama, D. C. Ralph, and R. A. Buhrman, *Phys. Rev. Lett.* **106**, 036601 (2011).
- [18] W. Zhang, M. B. Jungfleisch, F. Freimuth, W. Jiang, J. Sklenar, J. E. Pearson, J. B. Ketterson, Y. Mokrousov, and A. Hoffmann, *Phys. Rev. B* **92**, 144405 (2015).
- [19] V. E. Demidov, S. Urazhdin, H. Ulrichs, V. Tiberkevich, A. Slavin, D. Baither, G. Schmitz, and S. O. Demokritov, *Nat. Mater.* **11**, 1028 (2012).
- [20] A. Hamadeh, O. d'Allivy Kelly, C. Hahn, H. Meley, R. Bernard, A. H. Molpeceres, V. V. Naletov, M. Viret,

- A. Anane, V. Cros, S. O. Demokritov, J. L. Prieto, M. Muñoz, G. de Loubens, and O. Klein, *Phys. Rev. Lett.* **113**, 197203 (2014).
- [21] D. Steiauf and M. Fähnle, *Phys. Rev. B* **72**, 064450 (2005).
- [22] A. Brataas, Y. Tserkovnyak, and G. E. W. Bauer, *Phys. Rev. Lett.* **101**, 037207 (2008).
- [23] M. Fähnle, D. Steiauf, and J. Seib, *J. Phys. D* **41**, 164014 (2008).
- [24] K. Gilmore, M. D. Stiles, J. Seib, D. Steiauf, and M. Fähnle, *Phys. Rev. B* **81**, 174414 (2010).
- [25] C. Vittoria, S. D. Yoon, and A. Widom, *Phys. Rev. B* **81**, 014412 (2010).
- [26] W. Platow, A. N. Anisimov, G. L. Dunifer, M. Farle, and K. Baberschke, *Phys. Rev. B* **58**, 5611 (1998).
- [27] G. Woltersdorf and B. Heinrich, *Phys. Rev. B* **69**, 184417 (2004).
- [28] K. Lenz, H. Wende, W. Kuch, K. Baberschke, K. Nagy, and A. Jánossy, *Phys. Rev. B* **73**, 144424 (2006).
- [29] K. Zakeri, J. Lindner, I. Barsukov, R. Meckenstock, M. Farle, U. von Hörsten, H. Wende, W. Keune, J. Rucker, S. S. Kalarickal, K. Lenz, W. Kuch, K. Baberschke, and Z. Frait, *Phys. Rev. B* **76**, 104416 (2007).
- [30] L. Chen, S. Mankovsky, S. Wimmer, M. A. W. Schoen, H. S. Körner, M. Kronseder, D. Schuh, D. Bougeard, H. Ebert, D. Weiss, and C. H. Back, *Nat. Phys.* **14**, 490 (2018).
- [31] Q. Qin, S. He, H. Wu, P. Yang, L. Liu, W. Song, S. J. Pennycook, and J. Chen, [arXiv:1804.00554](https://arxiv.org/abs/1804.00554).
- [32] M. A. W. Schoen, D. Thonig, M. L. Schneider, T. J. Silva, H. T. Nembach, O. Eriksson, O. Karis, and J. M. Shaw, *Nat. Phys.* **12**, 839 (2016).
- [33] A. J. Lee, J. T. Brangham, Y. Cheng, S. P. White, W. T. Ruane, B. D. Esser, D. W. McComb, P. C. Hammel, and F. Yang, *Nat. Commun.* **8**, 234 (2017).
- [34] G. Chen, J. Zhu, J. Li, F. Z. Liu, and Y. Z. Wu, *Appl. Phys. Lett.* **98**, 132505 (2011).
- [35] M. B. Jungfleisch, W. Zhang, J. Sklenar, W. Jiang, J. E. Pearson, J. B. Ketterson, and A. Hoffmann, *Phys. Rev. B* **93**, 224419 (2016).
- [36] See Supplemental Material at <http://link.aps.org/supplemental/10.1103/PhysRevLett.122.117203> for a detailed description of the device geometry, high frequency ferromagnetic resonance and first-principles calculations, which includes Refs. [37–38].
- [37] C. Ciccarelli, K. M. D. Hals, A. Irvine, V. Novak, Y. Tserkovnyak, H. Kurebayashi, A. Brataas, and A. Ferguson, *Nat. Nanotechnol.* **10**, 50 (2015).
- [38] S. S. A. Razee, J. B. Staunton, B. Ginatempo, E. Bruno, and F. J. Pinski, *Phys. Rev. B* **64**, 014411 (2001).
- [39] K. Shikada, M. Ohtake, F. Kirino, and M. Futamoto, *J. Appl. Phys.* **105**, 07C303 (2009).
- [40] T. Kuschel, J. Hamrle, J. Pištora, K. Saito, S. Bosu, Y. Sakuraba, K. Takanashi, and J. Wollschläger, *J. Phys. D* **45**, 205001 (2012).
- [41] M. Farle, *Rep. Prog. Phys.* **61**, 755 (1998).
- [42] X. Liu, Y. Sasaki, and J. K. Furdyna, *Phys. Rev. B* **67**, 205204 (2003).
- [43] Y. Tserkovnyak, A. Brataas, and G. E. W. Bauer, *Phys. Rev. Lett.* **88**, 117601 (2002).
- [44] A. Ghosh, J. F. Sierra, S. Auffret, U. Ebels, and W. E. Bailey, *Appl. Phys. Lett.* **98**, 052508 (2011).
- [45] W. Zhang, M. B. Jungfleisch, W. Jiang, Y. Liu, J. E. Pearson, Suzanne G. E. te Velthuis, A. Hoffmann, F. Freimuth, and Y. Mokrousov, *Phys. Rev. B* **91**, 115316 (2015).
- [46] M. Caminale, A. Ghosh, S. Auffret, U. Ebels, K. Ollefs, F. Wilhelm, A. Rogalev, and W. E. Bailey, *Phys. Rev. B* **94**, 014414 (2016).
- [47] H. Suhl, *Phys. Rev.* **97**, 555 (1955).
- [48] S. Mizukami, Y. Ando, and T. Miyazaki, *Jpn. J. Appl. Phys.* **40**, 580 (2001).
- [49] V. Kamberský, *Can. J. Phys.* **48**, 2906 (1970).
- [50] V. Kamberský, *Phys. Rev. B* **76**, 134416 (2007).
- [51] K. Gilmore, Y. U. Idzerda, and M. D. Stiles, *Phys. Rev. Lett.* **99**, 027204 (2007).
- [52] S. S. A. Razee, J. B. Staunton, B. Ginatempo, F. J. Pinski, and E. Bruno, *Phys. Rev. Lett.* **82**, 5369 (1999).
- [53] Y. Kota and A. Sakuma, *Appl. Phys. Express* **5**, 113002 (2012).
- [54] I. Turek, J. Kudrnovský, and K. Carva, *Phys. Rev. B* **86**, 174430 (2012).
- [55] T. McGuire and R. Potter, *IEEE Trans. Magn.* **11**, 1018 (1975).
- [56] R. I. Potter, *Phys. Rev. B* **10**, 4626 (1974).